

International Journal of Optomechatronics

ISSN: (Print) (Online) Journal homepage: www.tandfonline.com/journals/uopt20

Large deflection angle resonant 1D scanning micromirror fabricated with multi jet fusion 3D printed parts

Wookyung Kim, Jeong-Yeon Hwang & Chang-Hyeon Ji

To cite this article: Wookyung Kim, Jeong-Yeon Hwang & Chang-Hyeon Ji (2024) Large deflection angle resonant 1D scanning micromirror fabricated with multi jet fusion 3D printed parts, International Journal of Optomechatronics, 18:1, 2371289, DOI: 10.1080/15599612.2024.2371289

To link to this article: https://doi.org/10.1080/15599612.2024.2371289

© 2024 The Author(s). Published with license by Taylor & Francis Group, LLC

Published online: 11 Jul 2024.

Submit your article to this journal

Article views: 253

View related articles

View Crossmark data

Citing articles: 1 View citing articles

Full Terms & Conditions of access and use can be found at https://www.tandfonline.com/action/journalInformation?journalCode=uopt20

INTERNATIONAL JOURNAL OF OPTOMECHATRONICS
2024, VOL. 18, NO. 1, 2371289
https://doi.org/10.1080/15599612.2024.2371289

Taylor & Francis
Taylor & Francis Group

OPEN ACCESS Check for updates

Large deflection angle resonant 1D scanning micromirror fabricated with multi jet fusion 3D printed parts

Wookyung Kim[a], Jeong-Yeon Hwang[b], and Chang-Hyeon Ji[a,b]

[a]Graduate Program in Smart Factory, Ewha Womans University, Seoul, Korea; [b]Department of Electronic and Electrical Engineering, Ewha Womans University, Seoul, Korea

ABSTRACT

This paper presents a one-dimensional scanning micromirror, utilizing Multi Jet Fusion three-dimensional (3D) printed polyamide 12 as its core material, with a gold-coated silicon mirror in a half-circle extension shape (4.2 mm × 15 mm). The micromirror serves as a horizontal scanner in a two-dimensional scan module for light detection and ranging. It features a self-supported coil for electromagnetic actuation, and its design is validated through analytical and finite element analyses. The magnetic circuit design is assessed with three magnet configurations. Forced air cooling and salt bath annealing processes are performed to mitigate the effect of Joule heating in the coil and improve the mechanical characteristics of the 3D printed structure. A maximum optical scan angle of 34° was achieved at 1,432 Hz with 90.8 mA_{rms} under forced air cooling. The salt bath annealing enhances the long-term reliability significantly, with a 12-hour operational test showing a 1.2% variation in resonant frequency.

KEYWORDS

Scanning micromirror; multi jet fusion; 3D printing; polyamide 12; light detection and ranging

1. Introduction

Light detection and ranging (LiDAR) is a technology that employs light rays to measure distance to target objects, which plays a crucial role in three-dimensional (3D) terrain and object scanning.[1] The time-of-flight (ToF) LiDAR sensor precisely measures the distance to a target object by measuring the time it takes for the laser pulse to be reflected off the target and return to the photodetector.[2–3] Widely applied in autonomous vehicles, robotics, drones, and terrain surveying,[4–6] this versatile technology has seen significant advancements, particularly with the integration of Microelectromechanical Systems (MEMS) scanning micromirrors into ToF LiDAR sensors.[7] Laser scanning optics, utilizing microfabricated scanning micromirrors, emerge as effective alternatives to motor-based counterparts in LiDAR systems. This shift is pivotal in downsizing and increasing the production rate of LiDAR systems, leading to significant cost reductions. Consequently, LiDAR technology is becoming more accessible and applicable across a broader range of industries.

MEMS technology has exhibited remarkable proficiency in creating compact devices.[8] Specifically, MEMS mirrors, engineered for compactness with substantial advantages in space utilization and high performance, make them particularly beneficial in delicate optical systems or portable devices. In contrast to traditional galvano or polygon mirrors, MEMS mirrors exhibit

CONTACT Chang-Hyeon Ji cji@ewha.ac.kr Ewha Womans University, 52 Ewhayeodae-gil, Seodaemun-gu, Seoul 03760, Korea.

© 2024 The Author(s). Published with license by Taylor & Francis Group, LLC
This is an Open Access article distributed under the terms of the Creative Commons Attribution-NonCommercial License (http://creativecommons.org/licenses/by-nc/4.0/), which permits unrestricted non-commercial use, distribution, and reproduction in any medium, provided the original work is properly cited. The terms on which this article has been published allow the posting of the Accepted Manuscript in a repository by the author(s) or with their consent.

Nomenclature

LiDAR	light detection and ranging	ABS	acrylonitrile butadiene styrene
3D	three-dimensional	PLA	polylactic acid
ToF	time-of-flight	PA12	polyamide 12
MEMS	microelectromechanical systems	2D	two-dimensional
AM	additive manufacturing	FOV	field of view
SLS	selective laser sintering	FEA	finite element analysis
SLA	stereolithography	Nd-Fe-B	neodymium-iron-boron
DLP	digital light processing	back emf	back electromotive force
MJF	multi jet fusion	FoM	figure-of-merit
FDM	fused deposition modeling		

enhanced durability and performance, including a high scan frequency due to the inherently small moment of inertia of the device.[9] Comprising miniature mechanical components, MEMS mirrors are smaller, lighter, and more resilient to micro-vibrations, ensuring stability and reliability over prolonged periods of use.[10] Despite the numerous advantages, traditional MEMS fabrication processes based on silicon substrates and semiconductor processing technology have drawbacks, including process complexity, the need for specialized and expensive equipment, a relatively long lead time, and limited material choices. An emerging manufacturing method garnering attention in various fields, including MEMS, is additive manufacturing (AM). The 3D printing technology facilitates the production of miniaturized and intricate 3D structures with simple processing steps, offering an alternative approach to address the limitations of conventional microfabrication.[11–12] Notably, 3D printing techniques such as selective laser sintering (SLS), stereolithography (SLA), digital light processing (DLP), Polyjet, and multi jet fusion (MJF) hold promise for fabricating various MEMS devices, benefiting from fast processing time while maintaining commendable dimensional accuracy and small feature size. The extensive range of materials available for 3D printing, encompassing resins, powders, and filaments based on polymers, ceramics, and metals, further enhances the value of the process.

A growing body of research has recently focused on developing MEMS scanning micromirrors through AM processes. MEMS scanning micromirrors fabricated with PolyJet,[13–14] SLS,[15] DLP,[16] MJF,[17] and fused deposition modeling (FDM)[18] 3D printers have been explored. The printing process incorporates various polymer materials, such as acrylonitrile butadiene styrene (ABS)-like resin, polylactic acid (PLA), VeroClear, and polyamide. As new applications, including LiDAR systems, emerge to benefit from MEMS scanning micromirrors, the performance requirements for these scanners become increasingly diverse. For example, scanning micromirrors designed for laser projection display and biomedical testing equipment typically require a mirror diameter in the 1 mm range and scan frequency in the tens of kilohertz. In contrast, LiDAR applications necessitate larger mirror sizes (3-7 mm) and lower scan frequencies (< 1 kHz), making them well-suited for AM-based scanning micromirror fabrication. Previously reported 3D printed MEMS scanning micromirrors exhibited resonant frequencies ranging from 84 to 415 Hz and mirror sizes from 9 to 400 mm^2.[13–18] In the conventional microfabrication approach, the total number of dies that can be fabricated on a single wafer decreases significantly with the increase in the size of the mirror. In contrast, the industrial 3D printer has a much larger build size, providing a distinct advantage in volume production. Furthermore, the typical lead time of the 3D printing process contributes to this advantage. Nevertheless, challenges persist in mechanical properties, including a relatively low Young's modulus, a highly negative temperature coefficient of Young's modulus, and insufficient printing resolution, all of which must be taken into account in the device design phase.[19–21]

This study focuses on developing a 1D electromagnetic scanning micromirror fabricated with the MJF 3D printing process. The core component of the device, excluding the externally

fabricated mirror plate, driving coil, and permanent magnets, is printed using polyamide 12 (PA12). While alternative methods such as SLS can be employed for 3D printing PA12, the MJF 3D printing process was chosen for its ability to create intricate 3D structures with high precision within a short production timeframe. The inherent nature of powder bed fusion 3D printing eliminates the need for support structures during printing, a critical factor when crafting delicate structures vulnerable to fracturing during the final support removal step. Furthermore, since MJF adopts a planar fusion approach rather than a point-by-point method, it facilitates a reduction in printing time and, consequently, the overall fabrication time of the device.[22] Previous research has demonstrated the viability of employing MJF 3D printing with PA12 for scanning micromirror fabrication. An omnidirectional scanning micromirror demonstrated an optical scan angle of 15.2° at 415 Hz in the horizontal scan mode and 14.5° at 406 Hz in the vertical scan mode.[17]

The target scanning micromirror is designed to serve as the slow scanner within a two-dimensional (2D) scan module based on two 1D scanners. As the slow scanner has to reflect the scan line generated by the fast scanner, a half-circle extension-shaped mirror is employed. The specified operational parameters for the proposed device are a target frequency range of 1-1.5 kHz and an optical scan angle of 30°. The primary thrust of this research lies in the fabrication of a MEMS scanner designed for LiDAR applications, featuring a large aperture size and field of view (FOV). The slow scanner in a 2D scan module must support forced mode actuation to generate a raster scan pattern, necessitating a very low first mode resonant frequency. However, achieving a high driving frequency is imperative to avoid resonance with surrounding vibrations.[23] Accordingly, it is assumed that the designed device will be employed in the Lissajous scan pattern generation using the target 2D scan module, as opposed to its raster scanning counterpart. For instance, specific requirements in a LiDAR system within an autonomous vehicle include a mirror size of at least 2 mm, a resonant frequency higher than 0.8 kHz for vibration immunity, and a FOV exceeding 25°.[24] While the developed device may not specifically target autonomous vehicle applications, stringent requirements across all aspects of mirror performance have been established to validate the feasibility of the proposed design and fabrication approach.

To achieve a high driving torque capable of overcoming the significant moment of inertia of the mirror while simultaneously maintaining a resonant frequency surpassing 1 kHz, an indirect electromagnetic actuation method, coupled with the amplification of angular deflection at resonance, has been employed. This technique has been widely used in the actuation of MEMS scanning micromirrors fabricated with silicon, where the driving coil is formed on the gimbal, and the rotation of the mirror is amplified at resonance.[25–29] The indirect actuation scheme was adopted in this research to address two primary concerns: achieving a sufficient optical scan angle at resonance and preventing heat-induced mirror distortion during actuation. A moving coil architecture was chosen over the moving magnet counterpart in implementing the indirect actuation. While electromagnetic actuation using a moving magnet inherently eliminates the possibility of temperature increase in the mobile part of the device during actuation, a moving coil architecture allows for generating a much more powerful magnetic field with stator magnets, owing to a higher degree of freedom in magnetic circuit design. Moreover, an increase in environmental temperature during operation remains unavoidable even with the moving magnet architecture. Consequently, we explored the impact of Joule heating in the driving coil on the characteristics of the fabricated MEMS scanning micromirror. In addition, the effect of salt bath annealing on the mechanical characteristics of the printed PA12 structure was analyzed by observing variations in driving characteristics. Considering the substantial questions raised about the reliability of using 3D printed polymers in MEMS device fabrication, a long-term reliability test was conducted to investigate optical scan angle and resonant frequency variations during continuous operation.

2. Materials and methods

2.1. 1D scanning micromirror design

In conventional MEMS scanning micromirrors, uniaxial or biaxial rotational motion of the reflective surface is employed to steer the beam in the desired direction. For a 2D scan, a single biaxial scanning micromirror or a combination of two uniaxial scanning micromirrors can be utilized (Figure 1). In general, the uniaxial scanning mirrors provide more stable motion compared to their biaxial counterparts, enabling more precise driving control and demonstrating increased resistance to shock and vibration. Despite these advantages, a 2D scan module based on uniaxial scanning micromirrors inherently faces challenges such as a larger volume requirement and the need for precise optical alignment of the two mirrors. In contrast, 2D scanning using a biaxial scanning micromirror offers advantages in terms of miniaturization, fabrication cost, reduced optical alignment burden, and overall system simplicity. However, careful consideration must be given to potential interference between the rotational motion along the two perpendicular scan axes and the higher distortion of the scanned 2D region during the design phase.

In this research, a 1D scanning micromirror has been developed as a horizontal scanner within a 2D laser scan module designed for LiDAR applications (Figure 1(*b*)). The target system comprises a fast-scanning micromirror with a 4 mm diameter, resonating at 6-7 kHz for the vertical scan, and a slow-scanning micromirror with a resonant frequency of 1-1.5 kHz for the horizontal scan. As the target FOV is $30^\circ \times 30^\circ$, the reflective surface of the slow scanner must cover the scan line generated by the fast scanner, featuring an optical scan angle of 30°. Therefore, a reflective surface with a larger dimension in the vertical direction becomes essential. The shape of the laser spot and scan line formed on the reflective surface depends critically on the incidence angle of the laser beam to the vertical scanner, the distance and relative angle between the two scanners, and the beam diameter. For simplicity, the shape variation of the laser spot and scan line due to incidence angle has been disregarded, considering only the radius of the laser beam incident on the fast scanner, the scan angle of the fast scanner, and the distance between the two scanners. Consequently, a scan line generated with a vertical scanner located at a distance of 20 mm, with an optical scan angle of 30°, can be effectively covered with a mirror dimension of 4.2 mm $\times$ 15 mm, providing a sufficient margin.

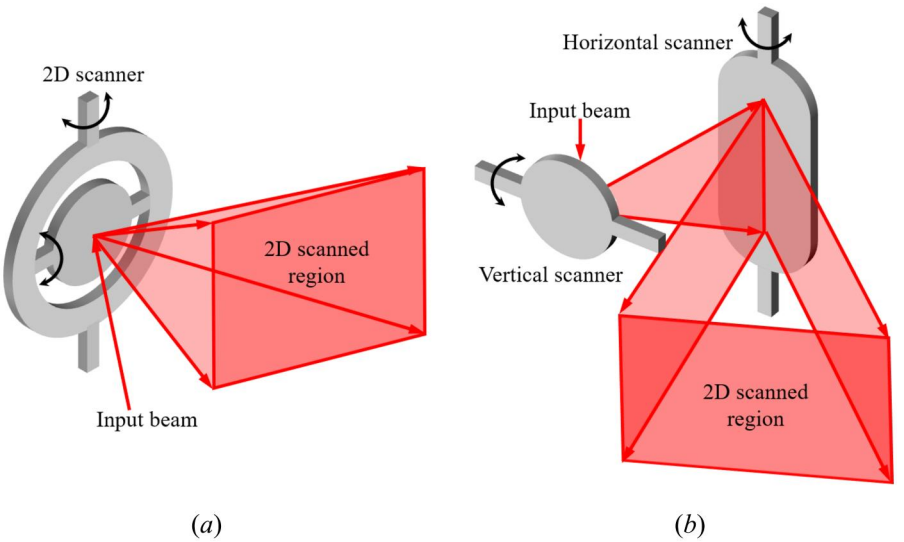


Figure 1. Schematic diagram of the various 2D scan approaches: (*a*) 2D scan using a single biaxial scanning micromirror, (*b*) 2D scan using two uniaxial scanning micromirrors.

The initial design of the proposed 1D scanning micromirror has been generated, considering the determined mirror plate size and indirect actuation scheme based on the driving coil integrated into the gimbal (Figure 2). All the structural layers except for the externally fabricated mirror plate and driving coil are composed of MJF 3D printed PA12. The minimum feature size and wall thickness suggested by the printing service provider (Red Solution, Seoul, Korea) is 600 μm. The detailed dimensions of the designed device are summarized in Table 1.

2.2. Modal analysis

Modal analysis was conducted using Ansys Workbench (Ansys, Inc., Canonsburg, PA, USA) to observe the actuation modes of the initial design. To better reflect the geometry and boundary condition of the device to be fabricated through a 3D printing process, the fixed end of the gimbal spring was extended to incorporate the actual support structure. During assembly with permanent magnets, securely attaching the fixed end of the spring to a housing or fixture is crucial for optimized performance. The material properties of the structural layers are outlined in Table 2.[30,31] As for the material property of copper, engineering data from Ansys Workbench was used with adjusted density to account for the copper fill-factor. As shown in Figure 3, the first

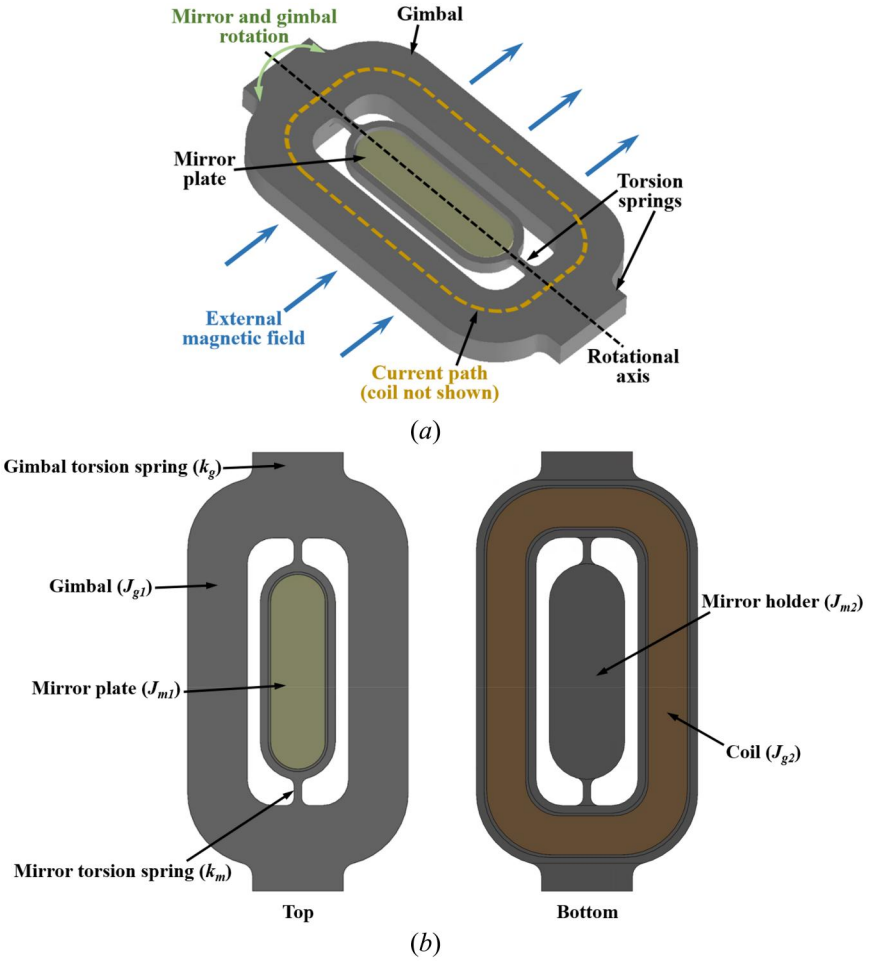


Figure 2. Designed 1D scanning micromirror: (*a*) perspective view and operation principle, (*b*) top and bottom side view and representative parameters of each part.

Table 1. Dimensions of the designed horizontal 1D scanning micromirror.

Parts		Dimension [unit]
Gimbal	Inner dimension	$10.8 \times 20.6\,mm^2$
	Outer dimension	$17 \times 29.8\,mm^2$
	Overall thickness	2.4 mm
	Torsion spring	$7.0 \times 2.2 \times 2.0\,mm^3$
Mirror	Mirror plate	$4.2 \times 15 \times 0.4\,mm^3$
	Mirror holder	$6.8 \times 16.6 \times 1.2\,mm^3$
	Torsion spring	$0.6 \times 2 \times 0.6\,mm^3$
Coil	Inner dimension	$9.4 \times 22.2\,mm^2$
	Outer dimension	$15.4 \times 28.2\,mm^2$
	Overall thickness	1.6 mm

Table 2. Material properties of the structural layers.

Material	Property	Value [unit]
Si	Density	2,330 [kgm^{-3}]
	Young's modulus	169 [GPa]
	Poisson's ratio	0.36
PA12	Density	1,010 [kgm^{-3}]
	Young's modulus	1.15 [GPa]
	Poisson's ratio	0.33
Copper	Density	6,061 [kgm^{-3}]
	Young's modulus	110 [GPa]
	Poisson's ratio	0.34

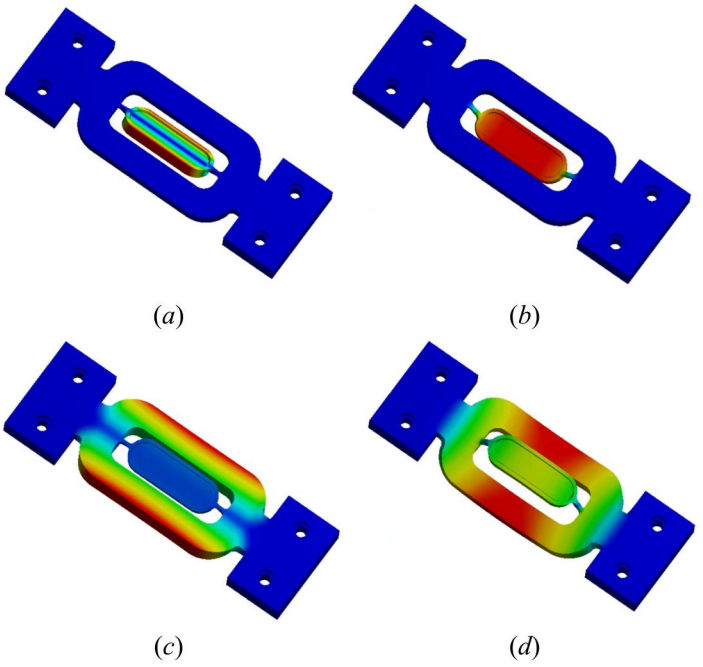


Figure 3. Modal analysis results of the initial model: (*a*) 1st mode at 827.1 Hz, (*b*) 2nd mode at 1,447.8 Hz, (*c*) 3rd mode at 1,518.6 Hz, (*d*) 4th mode at 2,250 Hz.

mode observed is the in-phase torsion mode at 827.1 Hz, wherein the mirror plate and gimbal rotate in phase. This first mode is the target mode, with the deflection angle of the mirror larger than that of the gimbal. The second mode identified is an in-phase piston mode at 1,447.8 Hz. The third mode corresponds to the out-of-phase torsion mode at 1,518.6 Hz, where the deflection angle of the gimbal is larger than that of the mirror. The fourth mode is an out-of-phase piston mode at 2,250 Hz. As the first mode resonant frequency falls significantly below the target range of 1-1.5 kHz, aligning the first mode resonant frequency with this range emerges as a major objective in the design optimization detailed in the subsequent chapters.

2.3. Analytical model and parametric analysis

The designed micromirror constitutes a series-connected two-spring-mass-damper system, incorporating various components such as the mirror plate and mirror holder, gimbal with an integrated coil, and torsion springs for the mirror and gimbal. The device can be effectively modeled using lumped elements, representing each component's moment of inertia, torsional spring constant, and damping constant. The rotational equations of motion are expressed in Equations (1) and (2).[29] Assuming zero initial condition for all deflection angles and angular velocities, the deflection angles of the mirror (θ_m) and the gimbal (θ_g) can be obtained through Laplace transform and simple matrix operations, as summarized in Equations (3) and (4). The parameters used in these equations are summarized in Table 3. The torsional spring constant is determined through static structural analysis using Ansys Workbench, and the moment of inertia is analyzed using SolidWorks (Dassault Systèmes SolidWorks Corporation, Waltham, MA, USA). The frequency response of the mirror deflection angle was analyzed to optimize the device design, employing an empirically determined damping coefficient.

$$J_m\ddot{\theta}_m + c_m\dot{\theta}_m + k_m\theta_m - c_m\dot{\theta}_g - k_m\theta_g = 0 \tag{1}$$

$$J_g\ddot{\theta}_g + (c_g + c_m)\dot{\theta}_g + (k_g + k_m)\theta_g - c_m\dot{\theta}_m - k_m\theta_m = T \tag{2}$$

$$\Theta_m(s) = \frac{(c_m s + k_m)T(s)}{(J_m s^2 + c_m s + k_m)(J_g s^2 + c_g s + c_m s + k_g + k_m) - (c_m s + k_m)^2} \tag{3}$$

$$\Theta_g(s) = \frac{(J_m s^2 + c_m s + k_m)T(s)}{(J_m s^2 + c_m s + k_m)(J_g s^2 + c_g s + c_m s + k_g + k_m) - (c_m s + k_m)^2} \tag{4}$$

Figure 4 shows the frequency response of θ_m and θ_g, obtained with the analytical solutions shown in Equations (3) and (4). As shown in Figure 4, the first rotational mode is observed at 917.5 Hz, and the second rotational mode at 2,944 Hz, corresponding to the first and third modes obtained through modal analysis using Ansys Workbench, respectively. Compared to the resonant frequencies obtained from modal analysis, the first mode resonant frequency was 11.1% higher, and that of the third mode was 93.9% higher. These discrepancies in resonant frequency are

Table 3. Parameters of the designed horizontal 1D scanning micromirror.

Symbol		Parameter	Value [unit]
J_m	J_{m1}	Moment of inertia of the mirror plate	2.18×10^{-10} [kgm^2]
	J_{m2}	Moment of inertia of the mirror holder	7.67×10^{-11} [kgm^2]
J_g	J_{g1}	Moment of inertia of the coil	1.16×10^{-8} [kgm^2]
	J_{g2}	Moment of inertia of the gimbal	6.82×10^{-11} [kgm^2]
k_m		Spring constant of the mirror	9.8×10^{-3} [Nm/rad]
k_g		Spring constant of the gimbal	24.6 [Nm/rad]
c_m		Damping coefficient of the mirror	10^{-9} [Nms/rad]
c_g		Damping coefficient of the gimbal	10^{-9} [Nms/rad]
T		Torque	10^{-6} [Nm]

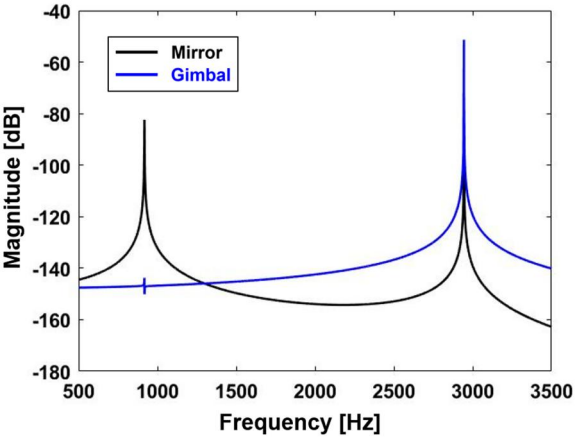


Figure 4. Frequency response of the initial model: (*a*) deflection angle of the mirror (black), (*b*) deflection angle of the gimbal (blue).

attributed to the non-ideal mechanical characteristics of the polymer-fabricated structures and an exceptionally large torsional spring constant of the gimbal spring. The relatively small Young's modulus of PA12 and small minimum wall thickness (0.6 mm) can cause printed structures to deform easily, deviating from ideal lumped element characteristics. In addition, the large width and high torsional spring constant of the gimbal spring may result in rotational motion resembling a bending of both ends in opposite directions rather than a pure rotation without structural deformation. Consequently, the discrepancy in resonant frequency is more significant for the third mode, where a substantial gimbal rotation occurs, as shown in Figure 4.

Although the analytical model revealed non-negligible discrepancies in the resonant frequency values when compared to finite element analysis (FEA) results summarized in Figure 3, a parametric analysis of two key parameters, torsional spring constants of the mirror (k_m) and the gimbal (k_g), was conducted to observe the trend in deflection angle variation. Given that the target mode (1st mode) exhibited relatively smaller errors, insights gained from the parametric analysis of the analytical model can contribute to understanding the resonance behavior of the designed device. Furthermore, parametric analysis results can be cross-verified with harmonic analysis results obtained through FEA. While it is true that modifying the moment of inertia of the gimbal (J_{g1}) and mirror holder (J_{m2}) could impact device performance, no shape changes have been considered for these parts. This decision is based on the understanding that increasing both the first mode resonant frequency and deflection angle at resonance would necessitate a reduction in the moment of inertia of these parts, potentially affecting the structure's rigidity and robustness. The two parameters, k_m and k_g, were varied, and the effect of the variation on the resonant frequency and deflection angle of the mirror was observed in the bode plot. Figure 5(*a*) shows the frequency response variation of the mirror deflection angle in response to changes in k_m. An increase in k_m results in higher resonant frequency and deflection angle. Conversely, an increase in k_g leads to a slight increase in resonant frequency and a decrease in the deflection angle (Figure 5(*b*)). The optimization aims to achieve the desired resonant frequency range and mode separation by adjusting these parameters, targeting frequencies between 1,000 and 1,500 Hz for the desired resonant frequency, and ensuring mode separation of at least 300 Hz.

2.4. Design optimization using harmonic analysis

As the analytical model is based on a lumped parameter model, assuming all structural components are rigid bodies, the actual behavior of the device is likely to be closer to the predictions

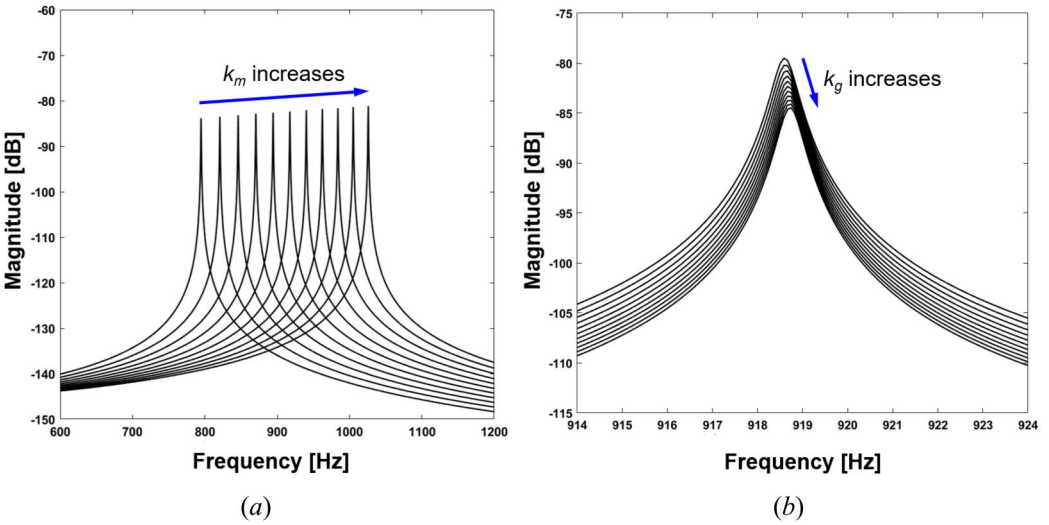


Figure 5. Effect of parameter variation on the frequency response of the mirror deflection angle: (*a*) k_m, (*b*) k_g.

obtained through FEA results using Ansys Workbench. Therefore, harmonic analysis using FEA was conducted to validate the frequency response variation trend obtained with the analytical model (Figure 5) and derive the final design. In the parametric analysis of the frequency response obtained with the analytical model, one parameter strongly correlated with the resonant frequency was the mirror spring constant (k_m). To increase the first mode resonant frequency from 827.1 Hz to the target frequency range (1-1.5 kHz) and improve the deflection angle, mirror spring thickness (t_m) was varied from 0.6 mm to 1 mm with a 0.1 mm step. The frequency response was analyzed through harmonic analysis using Ansys Workbench. The initial value of t_m is set at 0.6 mm, matching the minimum feature size of the MJF 3D printing process. As shown in Figure 6(*a*), the frequency response obtained with FEA exhibited trend similar to the analytical model. Increasing the mirror spring thickness, and thus the mirror spring constant, led to higher resonant frequency and increased deflection of the mirror. However, mode separation decreased as the mirror spring constant increased. Based on these results, a mirror spring thickness of 0.9 mm was selected, resulting in a first mode resonant frequency of 1,261.8 Hz and a second mode resonant frequency of 1,573.2 Hz. In this case, the second mode is the out-of-phase torsion mode, and the vertical deflection of the mirror in the first mode was 2.6 times larger than that of the initial model. The effect of changes in the gimbal spring constant (k_g) was also confirmed using FEA. Considering the designed thickness of the coil (1.6 mm) and minimum feature size, we set the total height of the gimbal at 2.4 mm, with the thickness of the gimbal spring set at 2.2 mm. Instead of changing the spring thickness, the width of the gimbal spring (w_g) was increased from 5 mm to 10 mm with a 1 mm step. In Figure 6(*b*), it is evident that the frequency response, as obtained through FEA, deviated from the trend observed in the analytical model (Figure 5(*b*)). The augmentation of the gimbal's spring constant resulted in a higher resonant frequency, displaying a substantial saturation beyond a w_g value of 6 mm. Initially, the mirror deflection exhibited an increase until the w_g reached 6 mm, after which it experienced a sharp decline. Notably, at a w_g value of 7 mm, the amplitude was more pronounced in the mirror mode, satisfying both the resonant frequency and mode separation requirements. However, at w_g values of 5 mm and 6 mm, mode separation fell below 150 Hz despite the significant deflection angle. In contrast to the frequency response obtained with the analytical model, changes in the gimbal spring constant resulted in a substantial change in the resonant frequency and deflection angle.

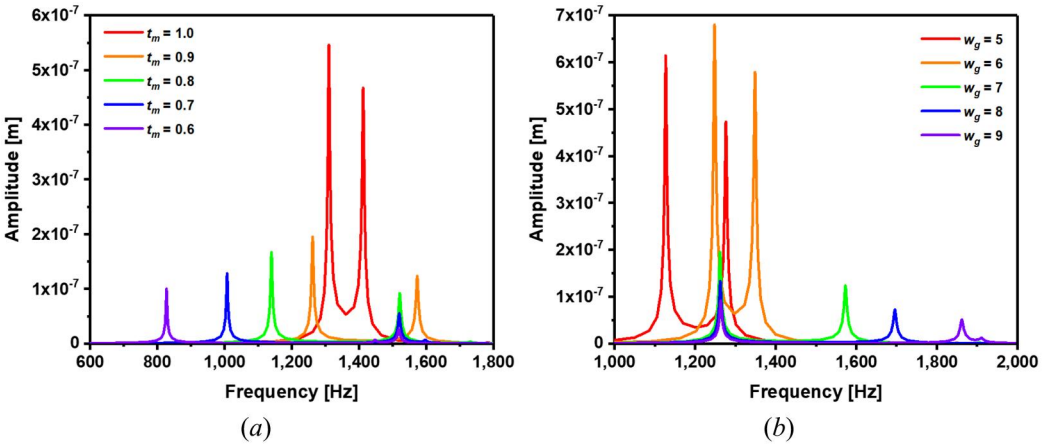


Figure 6. Effect of the variation of torsional spring constant on resonance modes obtained with Ansys Workbench: (*a*) effect of k_m variation due to thickness (t_m) variation, (*b*) effect of k_g variation due to width (w_g) variation.

Table 4 presents the optimized model's spring constant and moment of inertia values. As depicted in the modal analysis results shown in Figure 7, the first mode occurs at 1,261.8 Hz (in-phase torsion mode), the second mode at 1,573.2 Hz (out-of-phase torsion mode), and the third mode at 1,904.6 Hz (in-phase piston mode). The fourth mode is observed at 2,250 Hz (out-of-phase piston mode). Figure 8 compares the frequency responses of the initial and optimized models. The dotted and solid lines represent the frequency response of the initial and optimized micromirror designs, respectively. By comparing the two graphs, it is confirmed that the optimized model achieves a higher deflection of the mirror while attaining the resonant frequency between 1,000 and 1,500 Hz and maintaining mode separation above 300 Hz.

2.5. Magnetic circuit design

The designed device features a moving coil-type actuator, so a driving coil is integrated into the gimbal. A rectangular coil with rounded edges has been designed to fit within the slot formed at the bottom side of the gimbal. The inner and outer dimensions of the driving coil were $9.4 \times 22.2\,\text{mm}^2$ and $15.4 \times 28.2\,\text{mm}^2$, respectively. The total thickness of the coil was 1.6 mm. A copper wire with a 0.127 mm diameter was used, and the total number of turns was 276. When a wire with a length of L and current flow of I is situated inside the magnetic field with a flux density B, the total magnetic force acting on the wire (F_B) and the torque acting on the coil (T) can be obtained with Equations (5)-(7), where R is the distance between the origin and the center point of the coil's cross-section. The magnetic field must be applied perpendicular to the rotational axis to generate the rotational motion of the coil. Various magnet geometries have been compared to maximize the magnetic flux applied to the coil while minimizing the device volume. The magnetic circuit optimization was performed by FEA using Finite Element Method Magnetics (FEMM).[32]

First, the magnetic field intensity at the coil region for two different magnet configurations is compared (Figures 9(*a*)-(*b*)). In model #1 (Figure 9(*a*)), two magnets are located on both sides of the scanner, representing the most straightforward possible configuration but suffering from an inherent increase in the overall footprint of the device. In model #2 (Figure 9(*b*)), an array of four magnets is placed under the scanner with a back iron ($28.2 \times 30.4 \times 3\,\text{mm}^3$) at the bottom. This configuration utilizes the returning path of the magnetic flux formed between a pair of magnets magnetized vertically and has proven to be effective in generating a high lateral magnetic field near the magnetic poles exposed to air while maintaining a small footprint and volume for

Table 4. Comparison between the parameters of the initial and optimized model.

	Parameter		
Symbol	Initial model	Optimized model	Change
J_{m2}	2.18×10^{-10} [kgm^2]	2.18×10^{-10} [kgm^2]	None
J_{g2}	6.58×10^{-10} [kgm^2]	6.58×10^{-10} [kgm^2]	None
k_m	9.8×10^{-3} [Nm/rad]	2.05×10^{-2} [Nm/rad]	109% increase
k_g	24.6 [Nm/rad]	24.6 [Nm/rad]	None

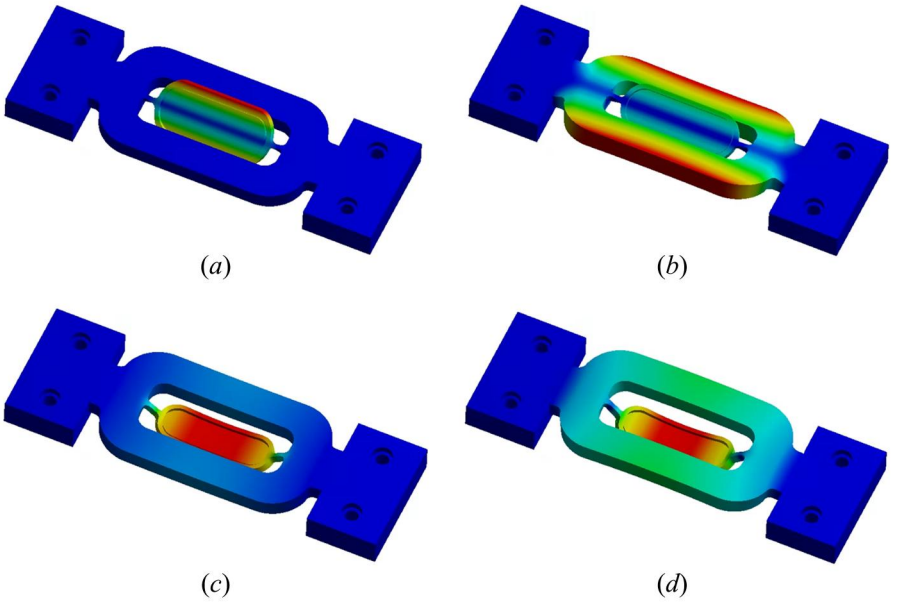


Figure 7. Modal analysis results of the optimized model: (*a*) 1st mode at 1,261.8 Hz, (*b*) 2nd mode at 1,523.2 Hz, (*c*) 3rd mode at 1,904.6 Hz, (*d*) 4th mode at 2,413 Hz.

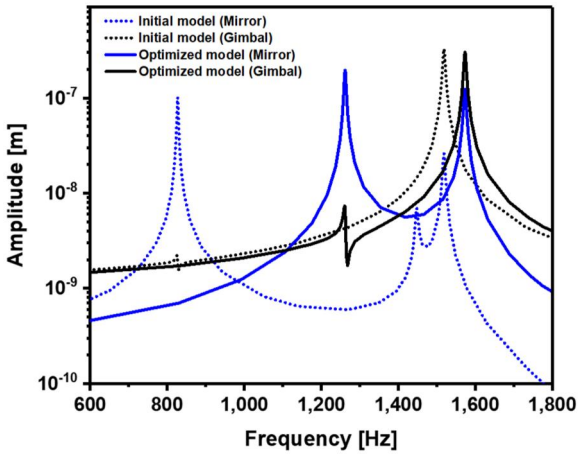


Figure 8. Frequency response comparison between the initial and optimized models (blue: maximum deflection of the mirror, black: maximum deflection of the gimbal).

electromagnetic MEMS scanning micromirrors.[26,27,29] The gap between the coil and the magnet surface is 2 mm and 2.6 mm for models #1 and #2, respectively. N42 grade neodymium-iron-boron (Nd-Fe-B) magnets with dimensions of $6.35 \times 25.4 \times 6.35$ mm^3 were used for both models.

The grade and dimension of the magnet were determined based on the availability. For comparison, we have analyzed the magnetic field intensity at the center line of the coil cross-section (red dotted line in Figure 9). The total width of the coil is 3 mm. As shown in Figure 10, lateral magnetic field intensity was slightly larger for model #2 in the left part of the coil region and larger for model #1 in the right part. Although model #2 provides higher lateral magnetic field intensity for a substantial part of the coil region, the increase in magnetic field compared to model #1 was not very large, considering that twice the number of magnets was used together with a back iron in model #2. Due to the relatively large mirror and gimbal size, a substantial gap had to be secured between the magnet and mirror plate, resulting in an overall decrease in the magnetic field intensity. As the magnet array placed under the scanner did not sufficiently improve the magnetic field intensity, model #1 was modified with increased magnet volume and tested (model #3, Figure 9(*c*)). The size of the new magnet was $12.7 \times 38.1 \times 12.7\,\text{mm}^3$. The size of the magnet was increased to both increase the lateral field intensity and supply a uniform magnetic field during the coil rotation. For model #3, the magnetic field intensity was increased by 90.9% from 110.3 kA/m (model #1) to 210.5 kA/m at the left end of the coil region, despite the increased gap between the coil and the magnet surface of 3 mm. As summarized in Figure 10, the highest magnetic field intensity could be obtained with model #3, which was utilized in the actuation of the fabricated device. However, an increase in overall device volume and footprint was unavoidable. The new magnet could not be used in the vertical magnet array configuration used in model #2 due to increased size. To fully utilize the lateral field in this configuration, the pitch of the coil (center-to-center distance of the two coil regions) should be close to twice the lateral dimension of the magnet, as shown in Figure 9(*b*).

$$\overrightarrow{F_B} = I\overrightarrow{L} \times \overrightarrow{B} \tag{5}$$

$$\overrightarrow{F_B} = \int_{x_0}^{x}\int_{y_0}^{y}\int_{z_0}^{z} \overrightarrow{J}(x,y,z,) \times \overrightarrow{B}(x,y,z)\ dxdydz \tag{6}$$

$$T = \overrightarrow{r} \times \overrightarrow{F_B} \cong 2RF_B \sin\theta \tag{7}$$

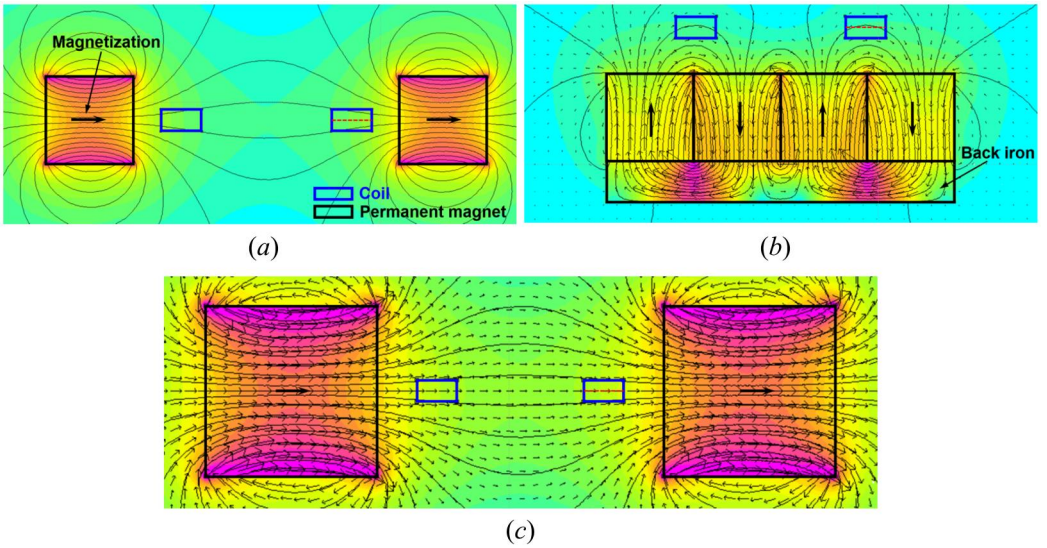


Figure 9. Magnetic field simulation results: (*a*) model #1, (*b*) model #2, (*c*) model #3.

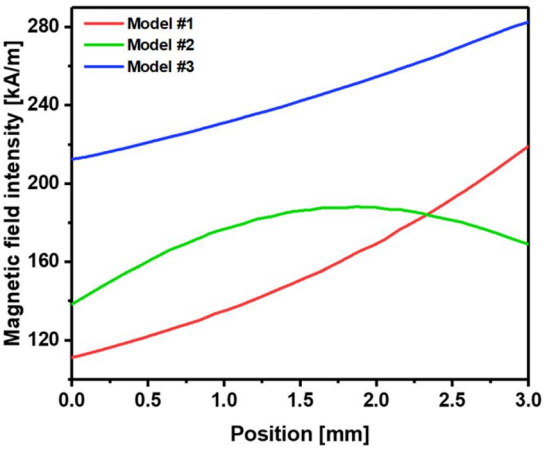


Figure 10. Magnetic field intensity in the coil region for models #1, #2, and #3.

3. Results and discussion

3.1. Fabrication and assembly results

The primary structural component of the device, encompassing the mirror holder and gimbal supported by torsion springs, was fabricated through the MJF 3D printing process, utilizing the HP Jet Fusion 3D 4200 (HP, Palo Alto, CA, USA). The structural layer material employed was PA12 (Figures 11(*a*)-(*b*)). The minimum feature size for the MJF 3D printing process was 0.6 mm. The 276-turn self-supported coil, depicted in Figure 11(*c*), was manufactured using copper wire with a diameter of 0.127 mm (Asung Tech, Gyeonggi-do, Korea). The mirror plate was prepared with a 400 um-thick silicon substrate via deep reactive ion etching (Withmems, Gyeonggi-do, Korea). The reflective surface measured 4.2 mm × 15 mm, featuring a corner radius of 2.1 mm. Chromium (10 nm) and gold (100 nm) layers were deposited as the reflective surface. The dimensional accuracy of the MJF 3D printed structure and the self-supported coil has been measured and analyzed. The thickness of the mirror torsion spring could not be measured directly due to insufficient clearance between the mirror holder and the gimbal. The dimensions were gauged using a digital vernier caliper (CD-15CPX, Mitutoyo Corp., Kawasaki, Japan) with an accuracy of ± 20 µm. As summarized in Table 5, the dimensional error of the printed structure ranged between 0.13-9.31%, with the maximum error observed in the gimbal thickness. Despite an occasional dimensional error of up to 9.31%, the overall accuracy proved acceptable, and the shape of the printed structure aligned well with the design. A maximum error of 6.28% was observed in the outer width for the coil dimension. The measured coil resistance was 41.8 Ω.

The 3D printed structure has been assembled with externally sourced components. Figure 12 shows the schematic representation of the packaged scanning micromirror. The mirror plate has been seamlessly inserted into the slot at the front side of the mirror holder and affixed securely using adhesive. At the same time, the self-supported coil has been carefully positioned within the slot on the rear side of the gimbal and secured with adhesive. In the final step of the assembly process, the 3D printed and assembled scanning micromirror was attached to the aluminum assembly fixture. Two N42 grade Nd-Fe-B magnets were employed, each possessing dimensions of $12.7 \times 38.1 \times 12.7\,\text{mm}^3$ (BX888, K&J Magnetics, Pipersville, PA, USA), identical to those utilized in the simulation of model #3. The magnets were aligned passively and inserted into the fixture. During the assembly of the 3D printed component, the fixed end of the printed structure was covered with an aluminum washer and miniature bolts and nuts were employed to fasten the structure securely (Figure 13). The total volume of the assembled device is $53.8 \times 48.8 \times 15.95\,\text{mm}^3$.

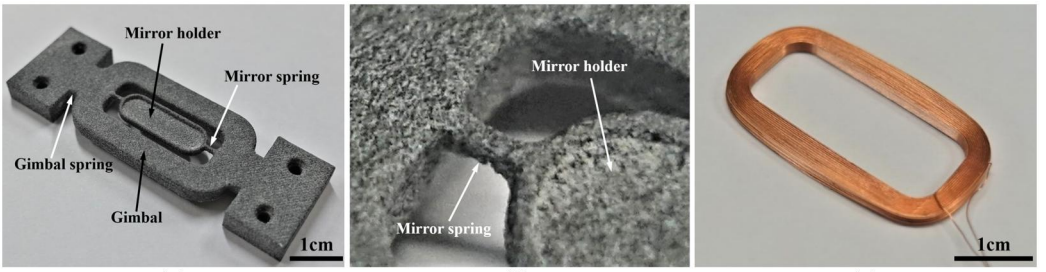


Figure 11. MJF 3D printed structure for 1D scanning micromirror: (*a*) perspective view, (*b*) magnified view of the mirror spring, (*c*) self-supported coil.

Table 5. Dimensions of the printed structure (average values obtained from three samples).

Part	Position	Designed value [mm]	Measured value (average) [mm]	Error [%]	Standard deviation [mm]
Gimbal	Inner length	20.6	20.6	0.13	0.02
	Inner width	7.8	7.8	0.17	0.04
	Outer length	29.8	29.9	0.28	0.02
	Outer width	17.0	17.1	0.39	0.02
	Overall thickness	2.4	2.6	9.31	0.04
Mirror holder	Length	16.6	16.6	0.30	0.11
	Width	5.8	5.8	0.69	0.02
	Overall thickness	1.2	1.1	4.72	0.01
Gimbal spring	Length	2.0	2.0	1.17	0.08
	Width	7.0	7.0	0.57	0.02
	Thickness	2.2	2.3	4.39	0.03
Mirror spring	Length	2.0	2.0	0.50	0.09
	Width	0.6	0.6	2.22	0.03
Coil	Inner length	22.2	22.1	0.68	0.04
	Inner width	9.4	9.5	1.42	0.06
	Outer length	28.2	27.7	1.89	0.17
	Outer width	15.4	14.4	6.28	0.37
	Thickness	1.6	1.5	3.33	0.02

3.2. 1D Scanning micromirror characterization

The optical measurement setup comprises a function generator (33500B, Keysight, Santa Rosa, CA, USA) and an amplifier (R300 plus, Inter-M Corp., Gyeonggi-do, Korea) for the generation of input current. A digital multimeter (Keysight 34461 A) is employed for current measurement. The setup also includes a fabricated 1D scanning micromirror and a laser diode. The function generator and the digital multimeter are connected to BenchVue software (Keysight), facilitating individual control of each piece of equipment and data extraction via a personal computer. The wavelength of the laser source is 638 nm. Upon driving the scanning micromirror, the laser beam incident on the mirror plate is reflected, generating a laser trajectory on the screen. The length of this laser trajectory on the screen is measured, and by considering the distance between the micromirror and the screen, the optical scan angle can be calculated. The formula for estimating the optical scan angle is shown in Equation (8), where θ_1 represents the optical scan angle, L_2 denotes the scan line length, and D_3 is the distance to the screen (Figure 14).

$$\theta_1 = 2\left(\tan^{-1}\frac{L_2}{2D_3}\right) \tag{8}$$

Initially, the resonance mode of the fabricated device was analyzed through a frequency sweep of the input current. Given that the designed device operates as a moving coil-type electromagnetic

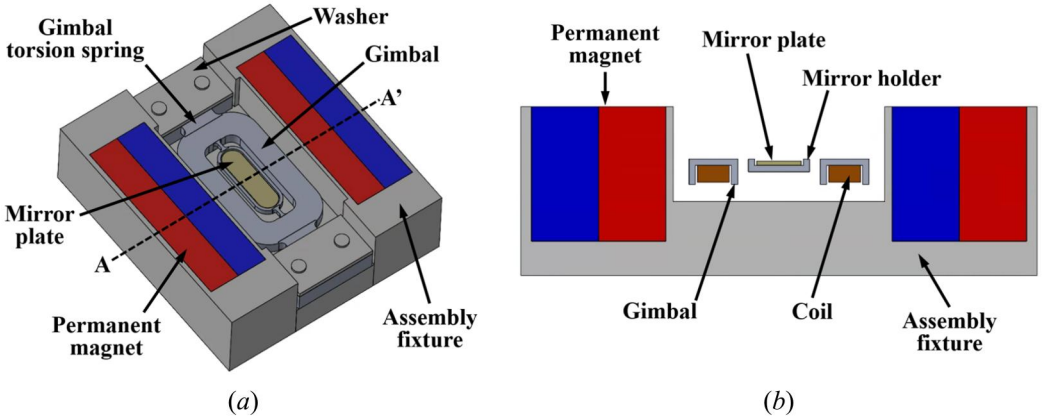


Figure 12. Schematic diagram of the scanning micromirror package: (*a*) perspective view of the assembled package, (*b*) cross-sectional view along line AA′ in (*a*).

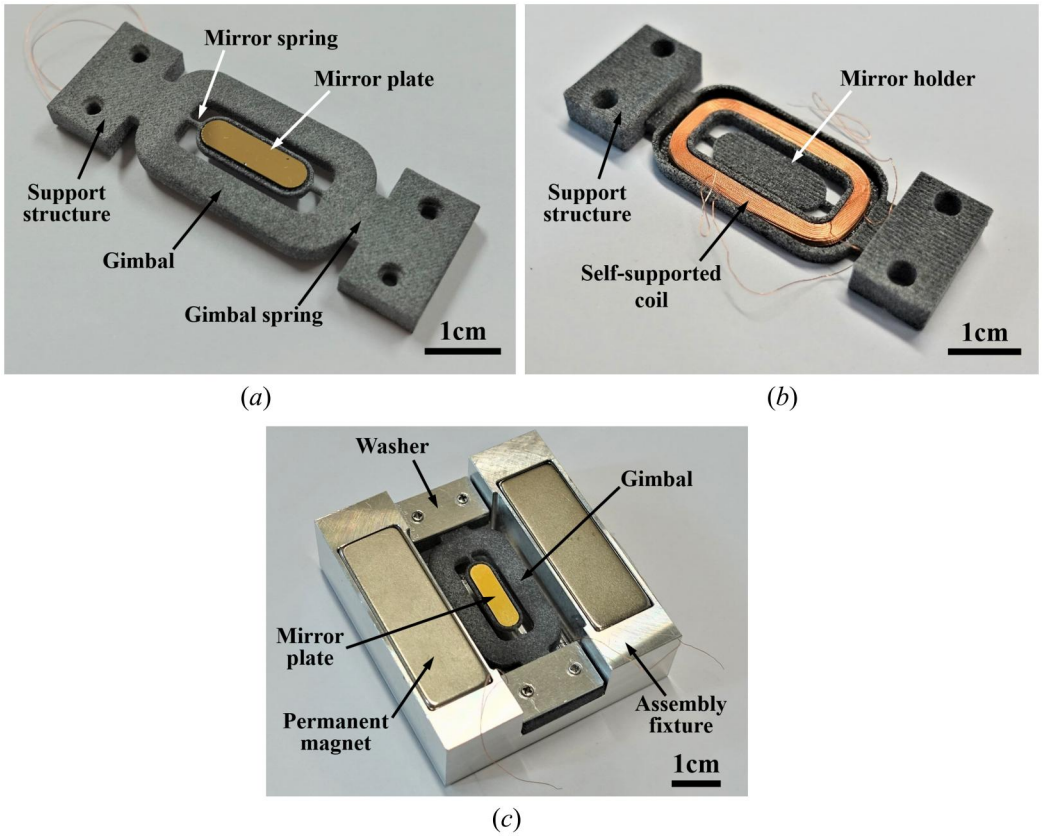


Figure 13. Assembled 1D scanning micromirror: (*a*) front-side of the 3D printed structure with integrated mirror plate, (*b*) back-side of the 3D printed structure with integrated coil, (*c*) fully packaged device in aluminum fixture.

actuator, back electromotive force (back emf) is generated at the coil during the actuation, leading to a reduction in the input current. Consequently, downward humps are observable in the input current graph at resonant frequencies due to the back emf generated during actuation. As the coil is attached to the gimbal, which undergoes a more extensive rotation during the out-of-phase

torsion mode compared to the in-phase counterpart, the back emf is notably larger for the second mode than the first mode. As shown in Figure 15, the fabricated 1D scanning micromirror exhibited a first mode (in-phase torsion mode) resonant frequency of 1,397 Hz and a second mode (out-of-phase torsion mode) resonant frequency of 1,600 Hz at an input current of 10 $mA_{rms.}$ According to FEA, the first and second mode resonant frequencies were anticipated to be 1,261.8 Hz and 1,573.2 Hz, respectively. Discrepancies between the FEA and measurement data were 10.7% and 1.70% for the first and second modes, respectively. These discrepancies are attributed to imperfections in the fabrication, errors in printed device dimensions, and mechanical properties utilized in the FEA, necessitating experimental validation. Resonant frequencies were measured while incrementing the input current in 20 mA_{rms} steps. The input current was set to the target value at the first mode resonance and fixed during each measurement. Despite decreased resonant frequency with increasing input current, mode shapes were consistently preserved, and the in-phase mirror torsion mode consistently maintained the first mode. This observation aligns with the FEA results obtained with Ansys Workbench. The measured resonant frequencies of the fabricated device at various input currents are summarized in Table 6.

The measured optical scan angle and first mode resonant frequency versus the input current are shown in Figure 16. The optical scan angle exhibited an increasing trend until reaching approximately 50 mA_{rms}. At that point, it began to saturate and decrease from around 70 mA_{rms} onwards. The maximum optical scan angle was 17° at 71.3 mA_{rms}, diminishing to 9° at 92.1 mA_{rms}. Beyond 92.1 mA_{rms}, the optical scan angle displayed an unstable trend, maintaining a relatively low scan angle near 8°. Simultaneously, the resonant frequency experienced a decrease of 400 Hz, declining from 1,397 Hz at 9.82 mA_{rms} to 997 Hz at 151.9 mA_{rms}. The observed diminishing trend in the optical scan angle with increasing current is presumed to be linked to temperature elevation in the coil region during actuation. In response, additional experiments were conducted to enhance the device's performance. Firstly, the temperature variation of the device during actuation was quantitatively measured, and the impact of forced air cooling using external

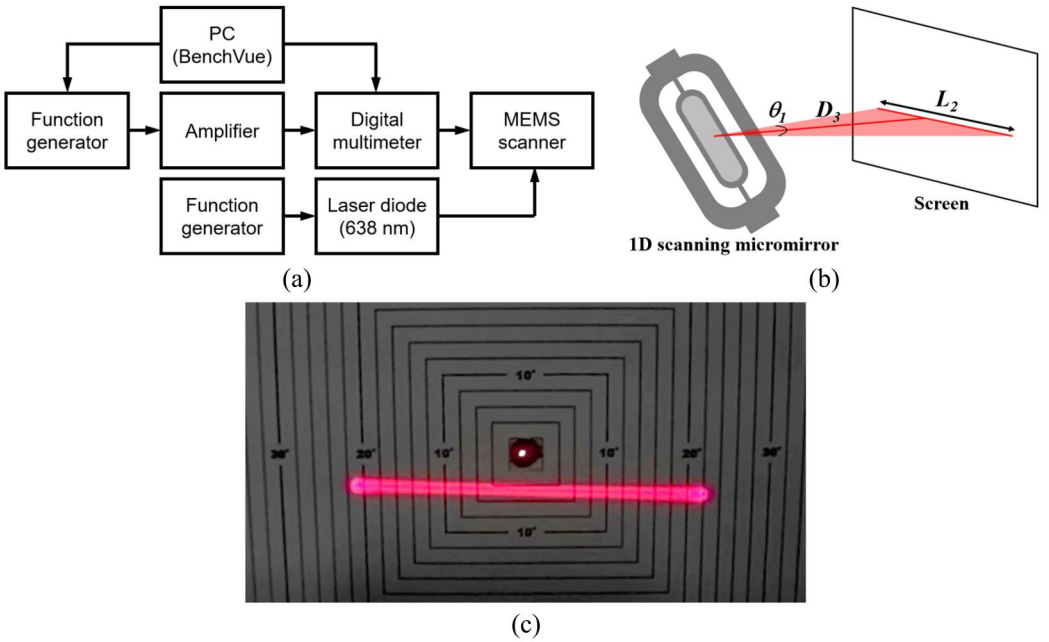


Figure 14. (*a*) block diagram of the measurement setup, (*b*) schematic diagram of the optical scan angle measurement method, (*c*) photograph of the scan line formed on the screen.

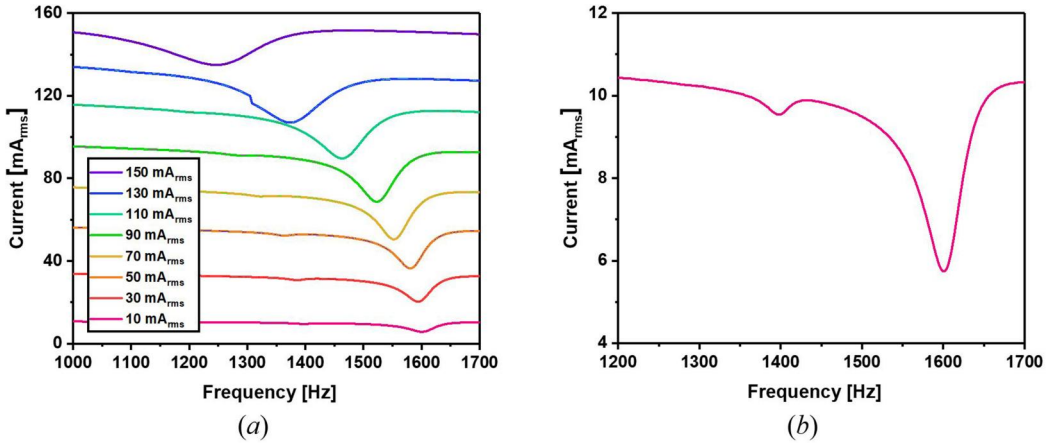


Figure 15. (*a*) driving current vs. frequency at various input levels, (*b*) magnified view of the driving current vs. frequency when the input current is 10 mA$_{rms}$.

Table 6. First and second mode resonant frequency at various input current.

Input current [mA$_{rms}$]	10	30	50	70	90	110	130	150
1st mode [Hz]	1,397	1,385	1,363	1,322	1,290	1,208	1,143	997
2nd mode [Hz]	1,600	1,594	1,581	1,552	1,523	1463	1,374	1,245

fans was analyzed. Secondly, a salt bath annealing process was implemented to improve the overall mechanical properties of the printed material.

3.3. Addressing joule heating-induced performance challenges

The temperature of the coil was monitored at various input currents using a thermal imaging camera (FLIR C3-X, Teledyne FLIR LLC, Wilsonville, Oregon, US), as shown in Figure 17. To evaluate the impact of temperature elevation during actuation, the optical scan angle was measured in the experimental setup both with and without the cooling system, comprising three cooling fans (Figure 18). As shown in Figure 19(*a*), the coil temperature increased to 81.1 °C at 150 mA$_{rms}$ without cooling, which was reduced to 42.1 °C when the cooling fans were activated. The optical scan angle at 90.8 mA$_{rms}$ input was increased from 8° to 34° due to cooling, ultimately achieving the maximum optical scan angle (Figure 19(*b*)), thereby confirming the influence of coil temperature on device performance. Additionally, the first mode resonant frequency increased from 997 Hz to 1,397 Hz at 150 mA$_{rms}$, and the resonant frequency drop decreased from 400 Hz to 160 Hz with the cooling system in operation (Figure 19(*c*)). For the uncooled device, a decrease in the optical scan angle was observed after 70 mA$_{rms}$ input, coinciding with a coil temperature of 38.6 °C. Conversely, the scan angle decrease occurred after 110 mA$_{rms}$ for the cooled device, corresponding to a temperature of 29.8 °C. While the precise temperature threshold at which the scan angle started to decrease could not be pinpointed, it can be inferred that the performance begins to deteriorate at approximately 30 to 40 °C.

The salt bath annealing process was conducted on the 3D printed structure to improve the mechanical properties of the printing material and mitigate the resonant frequency variation under increased input current. This post-processing method, commonly employed in AM, enhances the tensile strength of a 3D printed structure. Notably, it finds application in post-processing PLA structures generated through FDM 3D printing.[33] As the PLA is affected by high temperatures, an annealing method can be utilized to enhance the crystallinity and improve the mechanical properties.[34] Furthermore, the annealing of a PA12 structure generated using MJF 3D printing has been

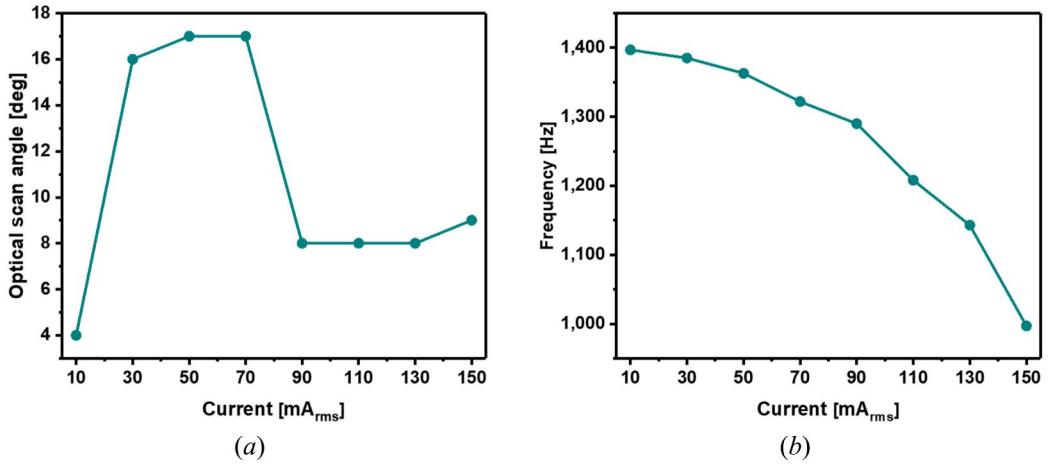


Figure 16. (*a*) optical scan angle vs. input current, (*b*) 1st mode resonant frequency vs. input current.

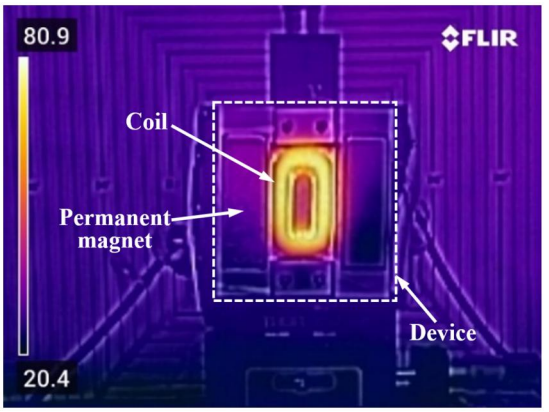


Figure 17. Images obtained with thermal imager (input current = 150 mA$_{rms}$).

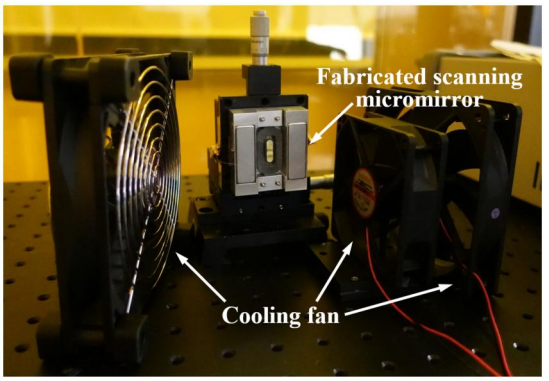


Figure 18. The cooling system consisting of three cooling fans.

demonstrated to enhance mechanical performances.[35] The annealing process was executed at 173 °C, positioned between the melting point and the glass transition temperature of PA12. The optimal ultimate tensile strength was achieved after 5 hours of annealing in the salt bath.

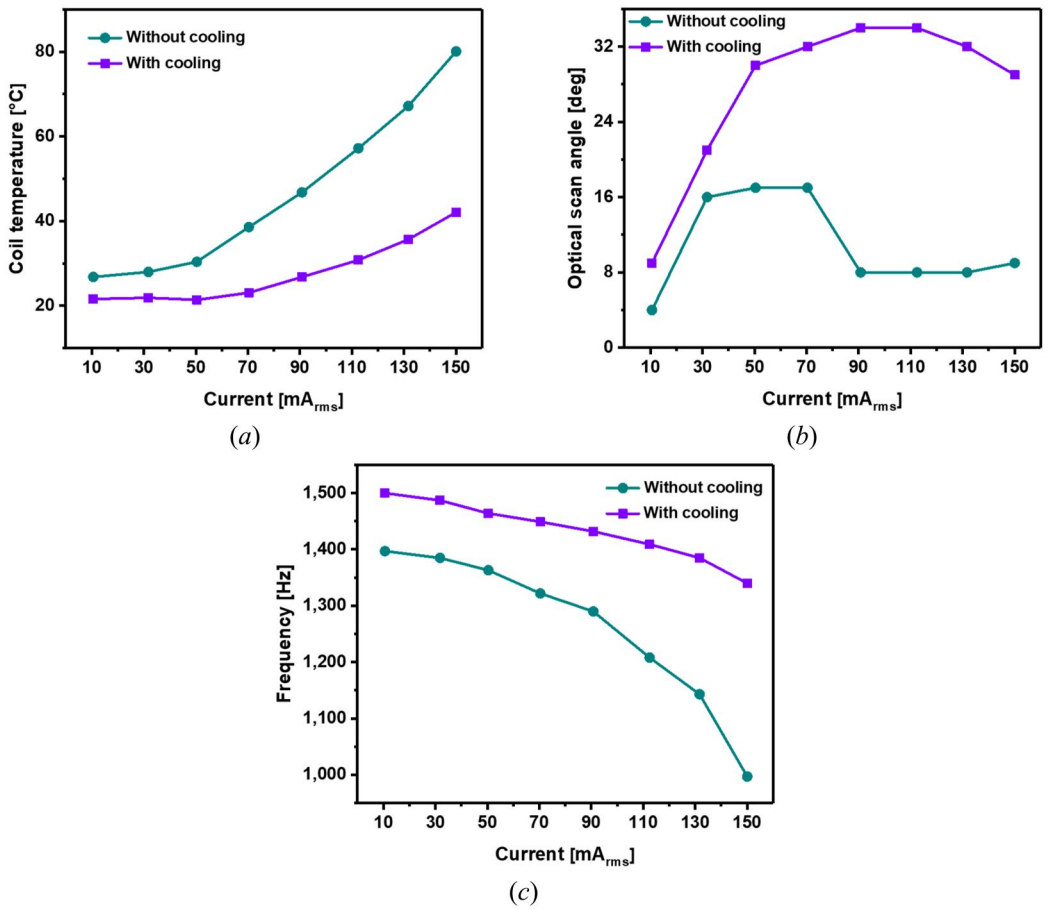


Figure 19. Measurement results of unannealed 1D scanning micromirror: (*a*) coil temperature vs. input current, (*b*) optical scan angle vs. current, (*c*) 1st mode resonant frequency vs. current.

The salt bath annealing process was conducted in a convection oven set at 173 °C, spanning durations from 1 to 7 hours in 2-hour increments. Throughout the annealing procedure, the 3D printed PA12 structure was immersed entirely in salt (Sempio fine sea salt, Sempio, Seoul, Korea) within a stainless steel container. Subsequently, the container was allowed to cool sufficiently at room temperature for 3 hours post-annealing. Figure 20 shows the variation of the first mode resonant frequency and optical scan angle versus input current, with an increase in annealing time. As shown in Figure 20, the sample subjected to an annealing time of 5 hours exhibited the smallest drop in resonant frequency and the largest optical scan angle, which agrees with prior research findings.[35] Nevertheless, a substantial decrease in resonant frequency and optical scan angle beyond 50 mA_{rms} of input current remained unresolved, which is a critical factor in optical scanning applications. Table 7 summarizes the first mode resonant frequency variation at two different input currents (10 and 150 mA_{rms}) with increased annealing time. As shown in Table 7, the first mode resonant frequency demonstrated an increasing trend until an annealing time of 3 hours, after which it started to saturate. The minimal resonant frequency drop, attributed to an increase in input current from 10 mA_{rms} to 150 mA_{rms}, was observed for an annealing time of 5 hours.

The 5 hour-annealed 1D scanning micromirror, demonstrating the most significant increase in optical scan angle compared to an unannealed device, underwent testing in a forced air cooling environment. As shown in Figure 21(*a*), the coil temperature was increased to 80.4 °C at

150 mA_{rms} without cooling, subsequently decreasing to 49.1 °C with the cooling fans activated. The first mode resonant frequency experienced an increase from 1,093 Hz to 1,265 Hz, and the resonant frequency dropped at 150 mA_{rms}, decreasing from 390 Hz to 213 Hz. The annealed and cooled sample achieved the maximum optical scan angle of 26° at 70 mA_{rms} input, in contrast to the 34° at 90 mA_{rms} observed for the unannealed and cooled device (Figure 19). Additionally, the optical scan angle exhibited a slight decrease after 70 mA_{rms}. The temperature at which the optical scan angle started to deteriorate was 35.6 °C for the uncooled device and 30.6 °C for the cooled device, with the trend not significantly deviating from that of the unannealed device. The decline in the maximum optical scan angle at resonance is attributed to the increased Young's modulus, confirmed by the increased resonant frequency. Considering that the device geometry and, consequently, the resonance behavior are optimized with mechanical properties provided by the supplier, an enhanced scanning performance could be achieved by taking the temperature-induced variation of the mechanical properties into account.

3.4. The long-term reliability

Up to the present, despite the development of various scanning micromirrors using different 3D printing methods and materials, the long-term reliability of printed polymer structures has yet to be examined thoroughly.[13–18] Moreover, the impact of salt bath annealing on the mechanical performance of an actuator device has not been explored. A comprehensive evaluation of the mechanical robustness of both the 5-hour annealed and unannealed 1D scanning micromirrors was undertaken through an extended reliability test conducted within a forced air cooling environment for 12 hours (Figure 22). The driving current was set to 50 mA_{rms}, and the optical scan angle at resonant frequency was measured. All experiments were conducted under standard laboratory conditions, with temperatures ranging from 20 °C to 25 °C and humidity levels maintained between 30% and 50%. Given that the number of operation cycles per unit time is contingent on the resonant frequency, it is noteworthy that the annealed device, with a higher resonant frequency, exhibited a slightly larger total number of cycles even after an identical test duration. The resonant frequency for the unannealed device decreased from 1,366 Hz to 1,223 Hz during the test. Throughout the test, the recorded maximum resonant frequency was 1,366 Hz, the minimum value was 1,223 Hz, and a frequency drop of 143 Hz was observed. The optical scan angle varied from 13° to 14°, with the maximum and minimum optical scan angles recorded as 14.5° and 9.5°, respectively.

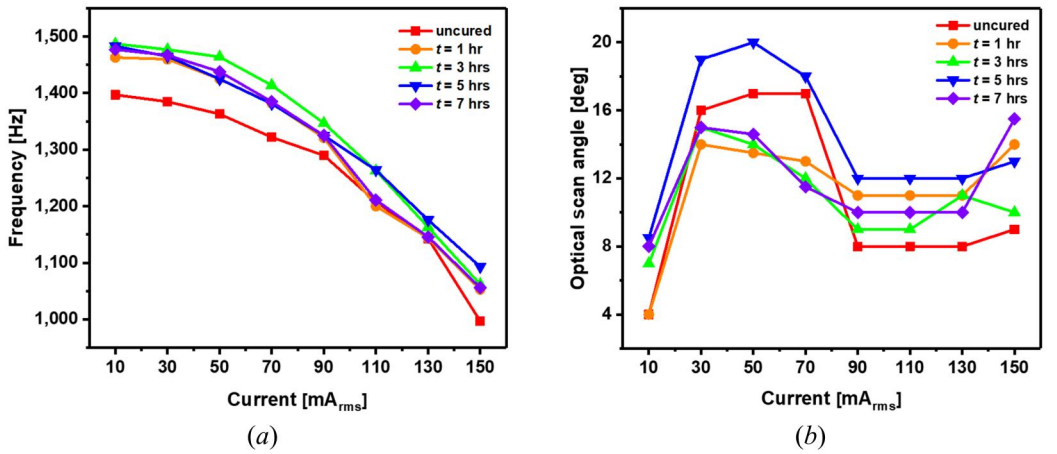


Figure 20. (*a*) 1st mode resonant frequency vs. input current for different annealing times, (*b*) optical scan angle vs. input current for different annealing time.

Table 7. Variation of 1st mode resonant frequency (f_1) at two different input currents (I) with an increase in annealing time.

Hours annealed	0	1	3	5	7
f_1 @ $I = 10\,mA_{rms}$ [Hz]	1,397	1,463	1,487	1,483	1,477
f_1 @ $I = 150\,mA_{rms}$ [Hz]	997	1,053	1,062	1,093	1,056
Resonant frequency drop [Hz]	400	410	425	390	421

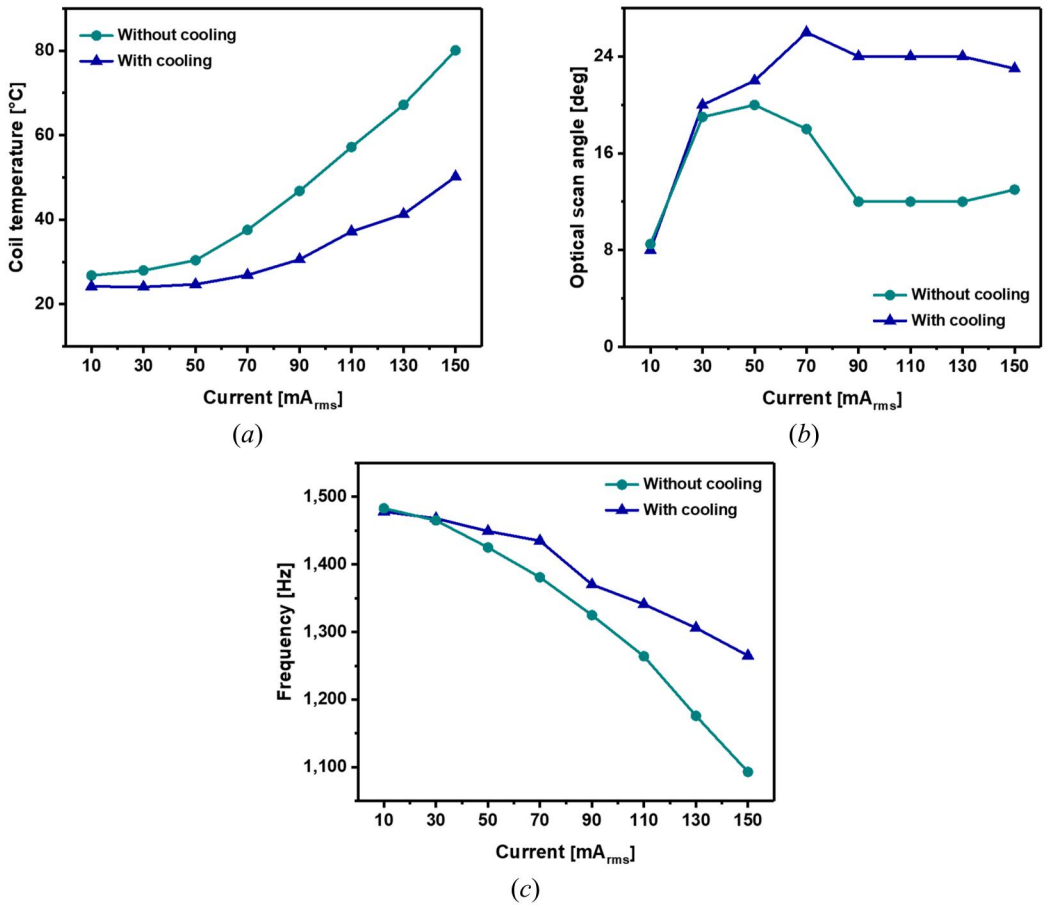


Figure 21. Measurement results of 5 hour-annealed 1D scanning micromirror: (*a*) coil temperature vs. input current, (*b*) optical scan angle vs. current, (*c*) 1st mode resonant frequency vs. current.

In summary, the unannealed device demonstrated an optical scan angle variation of 38.5% and a resonant frequency variation of 10.5% of the initial value. For the 1D scanning micromirror annealed for 5 hours, the resonant frequency increased from 1,453 Hz to 1,456 Hz after the test, with the maximum and minimum resonant frequencies recorded as 1,471 Hz and 1,453 Hz, respectively. The measured resonant frequency fluctuation was 18 Hz, accounting for 1.2% of the initial value. The optical scan angle increased from 18° to 19°, and the maximum and minimum optical scan angles during the measurement were 20° and 18°, respectively. The optical scan angle fluctuation was 2°, representing 11.1% of the initial value. As shown in Figure 22, the annealed device exhibited a higher optical scan angle and resonant frequency, and it did not show any signs of a decreasing trend for either parameter. This robust performance underscores the substantial improvement in the device's overall performance.

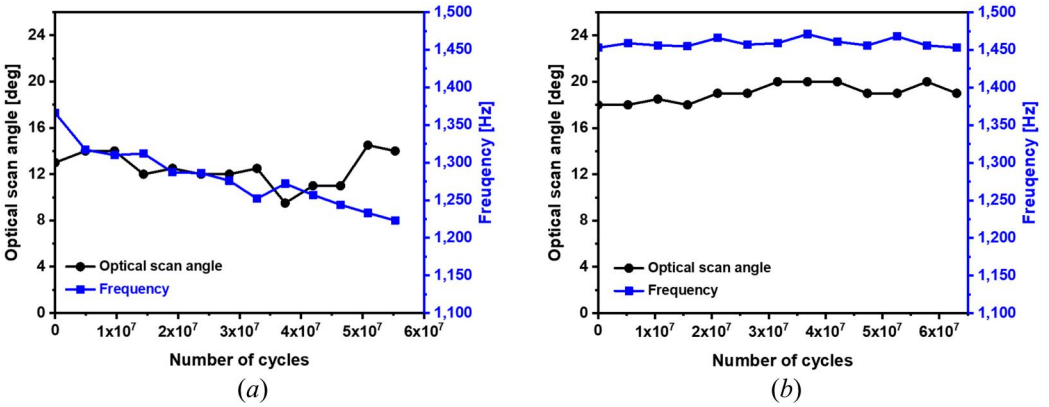


Figure 22. Long-term reliability test results: (*a*) unannealed device, (*b*) 5 hour-annealed device.

3.5. Summary and discussion

The performance of the developed scanning micromirror was benchmarked against previously reported scanners fabricated through the 3D printing process (Table 8). A key distinction lies in the substantially high resonant frequency of the developed device, which is an order of magnitude higher than its predecessors. To the author's knowledge, this marks the first implementation of a scanning micromirror fabricated with a 3D printed polymer as the structural layer material, achieving such a high scan frequency. Furthermore, the developed device boasted the largest optical scan angle compared to all previously reported devices. Table 8 compares two figure-of-merit (FoM) metrics established in the literature.[24] The first FoM is the product of the optical scan angle (θ) and effective mirror diameter (D), and the second FoM further includes the resonant frequency (f_r). As the scanner reported in[18] was not actuated at resonance, the FoM for this device was omitted. For 2D scanning micromirrors, FoMs were calculated for each scan axis, and maximum values were selected and compared.[13,15–17] As summarized in Table 8, the developed scanning micromirror exhibited at least 2.9 times higher θ·D product and 11.2 times higher θ·D·f_r product compared to the counterparts, underscoring the achievement of a large optical scan angle despite the large reflective surface area and high resonant frequency. Although not explicitly detailed in the performance comparison, the developed device demonstrated an optical scan angle variation of 11.1% and a resonant frequency variation of 1.2% of the initial value during the continuous actuation of 6.3×10^7 cycles.

In the design phase, the frequency response obtained from the analytical model of the device was compared with harmonic analysis results obtained through FEA to optimize device performance. Relatively high discrepancies between the analytical model and FEA were observed, a phenomenon not commonly encountered in devices fabricated with single crystal silicon.[26–29] This disparity may be attributed to the compliant nature (low Young's modulus) of the PA12 printed structures and the specific design of the gimbal spring. To enhance the accuracy of the device model employing lumped elements, a more comprehensive exploration of the structural deformation of the inertia element is essential. Additionally, while utilizing a material with a higher Young's modulus could be beneficial, the impact is expected to be relatively small considering the typical Young's modulus of polymer materials.

Despite the successful demonstration of optical scanning performance, further studies are required to enhance the thermal characteristics and explore the potential benefits of salt bath annealing. As outlined in the previous chapters, the maximum optical scan angle was attained with the device fabricated without salt bath annealing, whereas the 5-hour annealed sample exhibited markedly superior long-term reliability. The remelting during the salt bath annealing effectively reduced defects within the printed structure, such as void porosity, thereby enhancing

Table 8. Performance comparison of the previously reported 3D printed scanners and this work.

	This work	[13]	[15]	[16]	[17]	[18]
Scan type	1D	2D (Lissajous)	2D (Lissajous)	2D (spiral)	2D (spiral)	1D
Structural material	PA12	VeroClear	Polyamide	ABS-like	PA12	PLA
Fabrication	MJF	PolyJet	SLS	DLP	MJF	FDM
Actuation	EM	EM	EM	EM	EM	EM
Micromirror size [mm^2]	59.2* (4.2 × 15)	21 (7 × 3)	9 (3 × 3)	28.27 (ϕ6)	28.27 (ϕ6)	400 (20 × 20)
Effective diameter** (D) [mm]	8.7	5.2	3.4	6.0	6.0	22.6
Resonant frequency (f_r, H × V) [Hz]	1,432	315 × 180	305 × 105	309 × 308	415 × 406	84
Scan frequency (H × V) [Hz]	1,432	315 × 180	305 × 105	309 × 308	415 × 406	DC
Applied current [A_{rms}]	0.09	0.065	0.05	0.2	0.1	- (12 V)
FOV (θ, H × V) [°]	34	8 × 16	15 × 30	8.98 × 7.9	15.2 × 14.5	29.6
$(\theta \cdot D)_{max}$ [°mm]	295.3	82.8	101.6	53.9	91.2	–
$(\theta \cdot D \cdot f_r)_{max}$ [°mmHz]	422,812.6	14,895.9	15,490.9	16,651.9	37,854.7	–

*Half-circle extension-shaped.
**Equivalent diameter estimated with total area.

structural integrity and mechanical durability. However, since the designed device operates at resonance mode, where the amplification of angular deflection is critically dependent on mechanical properties such as Young's modulus and Poisson's ratio, changes in these properties resulting from annealing could potentially lead to a slight deterioration in the optical scan angle at resonance. Further investigations are needed to find a balance between optimizing mechanical properties through annealing and preserving the desired optical performance during resonance operation.

Developing a more compact yet powerful magnetic circuit is essential to enhance the device's performance further. This improvement would not only reduce the overall volume of the device but also lead to a reduction in the required driving current. Although the current device's performance has significantly improved with forced air cooling, there is room for further optimization by exploring a more stable material capable of withstanding high temperatures without a substantial decrease in Young's modulus. This strategy aims to ensure sustained device functionality even under elevated temperature conditions.

4. Conclusion

In this study, we successfully developed an electromagnetic 1D scanning micromirror using MJF 3D printed components as the core structural material. During the design phase of a horizontal scanner in a 2D scan module for LiDAR systems, we performed analytical modeling with a two-spring-mass-damper system and utilized FEA to optimize the device's design. To enhance driving torque, FEA analysis of the magnetic field intensity distribution in the coil region led to the development of an optimal design featuring two Nd-Fe-B magnets on both sides of the micromirror. The primary components of the micromirror, including the mirror, gimbal, and springs, were successfully fabricated using MJF 3D printing. These components were assembled with externally prepared elements, including the mirror plate, self-supported coil, and magnets, within an aluminum fixture. Following the observation of substantial degradation in optical scan angle and resonant frequency due to Joule heating in the coil, we implemented salt bath annealing and forced air cooling to address challenges associated with high input currents.

Forced air cooling effectively mitigated adverse effects of coil temperature increase during actuation. Experimental results confirmed the critical impact of coil temperature, with the optical scan angle showing signs of deterioration within the 30 to 40 °C range. The unannealed device achieved a maximum optical scan angle of 34° at 1,432 Hz with a 90.8 mA_{rms} input current, while the annealed device reached 26° at 1,435 Hz with a 70 mA_{rms} input current. The maximum optical scan angle was obtained with forced air cooling. Salt bath annealing, conducted at 173 °C

for varying durations, significantly improved the long-term reliability of the device. Extensive long-term reliability testing with forced air cooling confirmed that the annealed device maintained higher optical scan angles and resonant frequencies without exhibiting decreasing performance trends, even after enduring up to 6.3×10^7 cycles.

As a future direction, we recommend incorporating temperature-dependent mechanical properties into FEA for more accurate performance predictions. Despite substantial improvements in various aspects of the device's performance, including resonant frequency, optical scan angle, and long-term reliability, we recognize the potential for further enhancements in temperature dependence and optical scan angle. Utilizing materials with a smaller temperature coefficient of Young's modulus would be beneficial. The developed device and methodologies introduced in this study can be applied in various scanning micromirror applications, including LiDAR systems.

Disclosure statement

No potential conflict of interest was reported by the author(s).

Funding

This work was supported by the National Research Foundation of Korea (NRF) grant funded by the Korea government (MSIT) (2023R1A2C2004208, 2019M3C1B8090805), and by the BK21-Four Program.

References

[1] Wang, X.; Pan, H. Z.; Guo, K.; Yang, X.; Luo, S. The evolution of LiDAR and its application in high precision measurement. *IOP Conf. Ser: Earth Environ. Sci.* **2020**, *502*, 012008. DOI: 10.1088/1755-1315/502/1/012008.

[2] Grollius, S.; Ligges, M.; Ruskowski, J.; Grabmaier, A. Concept of an automotive LiDAR target simulator for direct time-of-flight LiDAR. *IEEE Trans. Intell. Veh.* **2023**, *8*, 825–835. DOI: 10.1109/TIV.2021.3128808.

[3] Niclass, C.; Ito, K.; Soga, M.; Matsubara, H.; Aoyagi, I.; Kato, S.; Kagami, M. Design and characterization of a 256x64-pixel single-photon imager in CMOS for a MEMS-based laser scanning time-of-flight sensor. *Opt. Express.* **2012**, *20*, 11863–11881. DOI: 10.1364/OE.20.011863.

[4] Wu, J.; Xu, H.; Zheng, J.; Zhao, J. Automatic vehicle detection with roadside LiDAR data under rainy and snowy conditions. *IEEE Intell. Transport. Syst. Mag.* **2021**, *13*, 197–209. DOI: 10.1109/MITS.2019.2926362.

[5] Gim, H.; Baek, S.; Park, J.; Lee, H.; Sung, C.; Kim, K.-T.; Ha, S. Suitability of various lidar and radar sensors for application in robotics: a measurable capability comparison. *IEEE Robot. Automat. Mag.* **2023**, *30*, 28–43. DOI: 10.1109/MRA.2022.3188213.

[6] Dogru, S.; Marques, L. Drone detection using sparse lidar measurements. *IEEE Robot. Autom. Lett.* **2022**, *7*, 3062–3069. DOI: 10.1109/LRA.2022.3145498.

[7] Mishra, M.; Dubey, V.; Mishra, P. M.; Khan, I. MEMS technology: a review. *JERR.* **2019**, *4*, 1–24. DOI: 10.9734/jerr/2019/v4i116891.

[8] Pattanaik, P.; Ojha, M. Review on challenges in MEMS technology. *Mater. Today: Proc.* **2023**, *81*, 224–226. DOI: 10.1016/j.matpr.2021.03.142.

[9] Yoo, H. W.; Druml, N.; Brunner, D.; Schwarzl, C.; Thurner, T.; Hennecke, M.; Schitter, G. MEMS-based lidar for autonomous driving. *Elektrotech. Inftech.* **2018**, *135*, 408–415. DOI: 10.1007/s00502-018-0635-2.

[10] Tadigadapa, S.; Nader, N. Reliability of micro-electro-mechanical systems (MEMS). *Proc. SPIE Conf.* **2001**, *4558*, 197–205. DOI: 10.1117/12.443002.

[11] Shirazi, S.; Gharehkhani, S.; Mehrali, M.; Yarmand, H.; Metselaar, H.; Kadri, N.; Osman, N. A Review on powder-based additive manufacturing for tissue engineering: selective laser sintering and inkjet 3D printing. *Sci. Technol. Adv. Mater.* **2015**, *16*, 033502. DOI: 10.1088/1468-6996/16/3/033502.

[12] Tan, L. J.; Zhu, W.; Zhou, K. Recent progress on polymer materials for additive manufacturing. *Adv. Funct. Materials* **2020**, *30*, 2003062–2003115. DOI: 10.1002/adfm.202003062.

[13] Savaş, J.; Khayatzadeh, R.; Çivitçi, F.; Gökdel, Y. D.; Ferhanoğlu, O. Toward fully three-dimensional-printed miniaturized confocal imager. *Opt. Eng.* **2018**, *57*, 1. DOI: 10.1117/1.OE.57.4.041402.

[14] Savaş, J.; Altınsoy, M.; Gökdel, Y. D.; Ferhanoğlu, O.; Çivitci, F. A 45° tilted 3D-printed scanner for compact side-view laser scanning endoscopy. *Microsyst. Technol.* **2020**, *26*, 1093–1099. DOI: 10.1007/s00542-019-04635-5.

[15] Gürcüoğlu, O.; Derman, I. D.; Altınsoy, M.; Khayatzadeh, R.; Çivitci, F.; Erten, A. C.; Ferhanoğlu, O. A 3D-printed 3D actuator for miniaturized laser scanning probes. *Sens. Actuator A Phys* **2021**, *317*, 112448–112456. DOI: 10.1016/j.sna.2020.112448.

[16] Seo, J.; Hwang, J.-Y.; Ji, C.-H. Electromagnetic 2D scanning micromirror fabricated with 3D printed polymer parts for LiDAR applications. *Sens. Actuator A Phys.* **2022**, *348*, 113997. DOI: 10.1016/j.sna.2022.113997.

[17] Hwang, J.; Seo, J.; Ji, C.-H. Electromagnetic omnidirectional scanning micromirror with multi jet fusion printed structures for smart factory applications. *Addit. Manuf.* **2022**, *55*, 102868. DOI: 10.1016/j.addma.2022.102868.

[18] Shen, C.-K.; Huang, Y.-N.; Liu, G.-Y.; Tsui, W.-A.; Cheng, Y.-W.; Yeh, P.-H.; Tsai, J.-C. Low-cost 3D-printed electromagnetically driven large-area 1-DOF optical scanners. *Photonics* **2022**, *9*, 484. DOI: 10.3390/photonics9070484.

[19] Zhou, C.; Guo, H.; Li, J.; Huang, S.; Li, H.; Meng, Y.; Yu, D.; Christiansen, J. C.; Jiang, S. Temperature dependence of poly(lactic acid) mechanical properties. *RSC Adv.* **2016**, *6*, 113762–113772. DOI: 10.1039/C6RA23610C.

[20] Li, J.; Jia, Y.; Li, T.; Zhu, Z.; Zhou, H.; Peng, X.; Jiang, S. Tensile behavior of acrylonitrile butadiene styrene at different temperatures. *Adv. Polym. Technol.* **2020**, (*2020*,)1–10. DOI: 10.1155/2020/8946591.

[21] Bai, J.; Goodridge, R. D.; Hague, R. J. M.; Song, M.; Okamoto, M. Influence of carbon nanotubes on the rheology and dynamic mechanical properties of polyamide-12 for laser sintering. *Polym. Test.* **2014**, *36*, 95–100. DOI: 10.1016/j.polymertesting.2014.03.012.

[22] Tey, W. S.; Cai, C.; Zhou, K. A comprehensive investigation on 3D printing of polyamide 11 and thermoplastic polyurethane via multi jet fusion. *Polymers. (Basel)* **2021**, *13*, 2139. DOI: 10.3390/polym13132139.

[23] Schlager, B.; Goelles, T.; Behmer, M.; Muckenhuber, S.; Payer, J.; Watzenig, D. Automotive lidar and vibration: resonance, inertial measurement unit, and effects on the point cloud. *IEEE Open J. Intell. Transp. Syst.* **2022**, *3*, 426–434. DOI: 10.1109/OJITS.2022.3176471.

[24] Wang, D.; Watkins, C.; Xie, H. MEMS mirrors for LiDAR: a review. *Micromachines. (Basel)* **2020**, *11*, 456–479. DOI: 10.3390/mi11050456.

[25] Ji, C.-H.; Choi, M.; Kim, S.-C.; Song, K.-C.; Bu, J.-U.; Nam, H.-J. Electromagnetic two-dimensional scanner using radial magnetic field. *J. Microelectromech. Syst.* **2007**, *16*, 989–996. DOI: 10.1109/JMEMS.2007.892897.

[26] Cho, A. R.; Han, A.; Ju, S.; Jeong, H.; Park, J.-H.; Kim, I.; Bu, J.-U.; Ji, C.-H. Electromagnetic biaxial microscanner with mechanical amplification at resonance. *Opt. Express.* **2015**, *23*, 16792–16802. [Mismatch DOI: 10.1364/OE.23.016792.

[27] Ju, S.; Jeong, H.; Park, J.-H.; Bu, J.-U.; Ji, C.-H. Electromagnetic 2D scanning micromirror for high definition laser projection displays. *IEEE Photon. Technol. Lett.* **2018**, *30*, 2072–2075. DOI: 10.1109/LPT.2018.2877303.

[28] Kang, S.; Park, J.; Ji, C.-H. Design optimization of a 6.4 mm-diameter electromagnetic 2D scanning micromirror. *Opt. Express.* **2020**, *28*, 31272–31286. DOI: 10.1364/OE.395903.

[29] Hwang, J.-Y.; Bu, J.-U.; Ji, C.-H. Low power electromagnetic scanning micromirror for LiDAR system. *IEEE Sensors J.* **2021**, *21*, 7358–7366. DOI: 10.1109/JSEN.2020.3048710.

[30] Hopcroft, M. A.; Nix, W. D.; Kenny, T. W. What is the young's modulus of silicon? *J. Microelectromech. Syst.* **2010**, *19*, 229–238. DOI: 10.1109/JMEMS.2009.2039697.

[31] Nazir, A.; Arshad, A.-B.; Hsu, C.-P.; Jeng, J.-Y. Effect of fillets on mechanical properties of lattice structures fabricated using multi-jet fusion technology. *Materials* **2021**, *14*, 2194–2201. DOI: 10.3390/ma14092194.

[32] Finite Element Method Magnetics. https://www.femm.info/wiki/HomePage.

[33] Szust, A.; Adamski, G. Using thermal annealing and salt remelting to increase tensile properties of 3D FDM prints. *Eng. Fail. Anal.* **2022**, *132*, 105932. DOI: 10.1016/j.engfailanal.2021.105932.

[34] Amza, C. G.; Zapciu, A.; Constantin, G.; Baciu, F.; Vasile, M. I. Enhancing mechanical properties of polymer 3D printed parts. *Polym* **2021**, *13*, 562. DOI: 10.3390/polym13040562.

[35] Liu, X.; Tey, W.; Choo, J.; Chen, J.; Tan, P.; Cai, C.; Ong, A.; Zhao, L.; Zhou, K. Enhancing the mechanical strength of multi jet fusion–printed polyamide 12 and its glass fiber-reinforced composite via high-temperature annealing. *Addit. Manuf.* **2021**, *46*, 102205. DOI: 10.1016/j.addma.2021.102205.